Biomaterials and Biosystems 13 (2024) 100087

Contents lists available at ScienceDirect

Biomaterials and Biosystems

journal homepage: www.elsevier.com/locate/bbiosy

3D printed hybrid scaffolds do not induce adverse inflammation in mice and direct human BM-MSC chondrogenesis *in vitro*

Silvia A. Ferreira [a,1,*], Francesca Tallia [b], Agathe Heyraud [b], Simone A. Walker [a], Christoph Salzlechner [c], Julian R. Jones [b], Sara M. Rankin [a]

[a] National Heart & Lung Institute, Imperial College London, London, UK
[b] Department of Materials, Imperial College London, London, UK
[c] Centre for Craniofacial and Regenerative Biology, King's College London, London, UK

ARTICLE INFO

Keywords:
3D printed hybrid scaffolds
Sterilisation
Subcutaneous implantation
Mesenchymal stem/stromal cells
Chondrogenesis

ABSTRACT

Biomaterials that can improve the healing of articular cartilage lesions are needed. To address this unmet need, we developed novel 3D printed silica/poly(tetrahydrofuran)/poly(ε-caprolactone) (SiO_2/PTHF/PCL-diCOOH) hybrid scaffolds. Our aim was to carry out essential studies to advance this medical device towards functional validation in pre-clinical trials. First, we show that the chemical composition, microarchitecture and mechanical properties of these scaffolds were not affected by sterilisation with gamma irradiation. To evaluate the systemic and local immunogenic reactivity of the sterilised 3D printed hybrid scaffolds, they were implanted subcutaneously into Balb/c mice. The scaffolds did not trigger a systemic inflammatory response over one week of implantation. The interaction between the host immune system and the implanted scaffold elicited a local physiological reaction with infiltration of mononuclear cells without any signs of a chronic inflammatory response.

Then, we investigated how these 3D printed hybrid scaffolds direct chondrogenesis *in vitro*. Human bone marrow-derived mesenchymal stem/stromal cells (hBM-MSCs) seeded within the 3D printed hybrid scaffolds were cultured under normoxic or hypoxic conditions, with or without chondrogenic supplements. Chondrogenic differentiation assessed by both gene expression and protein production analyses showed that 3D printed hybrid scaffolds support hBM-MSC chondrogenesis. Articular cartilage-specific extracellular matrix deposition within these scaffolds was enhanced under hypoxic conditions (1.7 or 3.7 fold increase in the median of aggrecan production in basal or chondrogenic differentiation media).

Our findings show that 3D printed SiO_2/PTHF/PCL-diCOOH hybrid scaffolds have the potential to support the regeneration of cartilage tissue.

Introduction

Adult articular cartilage has restricted inherent regenerative potential [1]. Injuries and progressive degenerative joint pathologies impair articular cartilage function, cause pain and disability to the patients and result in socio-economic burden [2]. For sports injury or trauma in young patients, the surgical best practice is microfracture, which involves drilling into the bone to liberate the marrow [3,4]. The aim is for the liberated bone marrow mesenchymal stem/stromal cells (BM-MSCs) to differentiate into chondrocytes and produce new cartilage. Unfortunately, the matrix that forms tends to be typical of the mechanically inferior fibrocartilage as opposed to the desired native hyaline cartilage, which means the repair can be short-lived. There are currently no treatments or strategies that robustly promote the long-term healing of articular cartilage lesions, preventing their progression to osteoarthritis.

One strategy is the creation of medical devices with specific biomaterials that can be used in combination with microfracture [1]. While layered fibremat-like collagen scaffolds initially held promise, clinical trials indicated they were no more successful than microfracture alone with long-term success remaining in doubt, due to their tendency to promote the formation of fibrocartilage [5–7]. The ideal scaffold would provide the biochemical and mechanical cues that stimulate

* Corresponding author at: National Heart & Lung Institute, Faculty of Medicine, Imperial College London, South Kensington Campus, London SW7 2AZ, UK.
E-mail address: silvia.ferreira@i3s.up.pt (S.A. Ferreira).
[1] Present Address: i3S - Instituto de Investigação e Inovação em Saúde, Universidade do Porto, Rua Alfredo Allen, 208. 4200-135 Porto, Portugal.

https://doi.org/10.1016/j.bbiosy.2024.100087
Received 10 October 2023; Received in revised form 26 December 2023; Accepted 8 January 2024
Available online 8 January 2024

chondrogenesis of hBM-MSCs promoting the production of hyaline cartilage extracellular matrix (ECM), increasing cartilage formation and reducing hypertrophy [8–10].

Recently, we developed 3D printed hybrids of silica, poly(tetrahydrofuran) (PTHF) and poly(ε-caprolactone) (PCL-diCOOH). We have shown that these scaffolds have similar mechanical properties to cartilage and can withstand cyclic loading [11]. Sol-gel hybrids are co-networks of inorganic (*e.g.,* silica) and organic components in which mechanical properties and dissolution rate can be tailored through the degree of covalent coupling between the inorganic and organic networks [12–14]. Without any such bonding, hybrids would dissociate rapidly in contact with water [15]. Additionally, the 3D pore architecture present within scaffolds has also been shown to play a vital role in tissue formation [10,16,17] and 3D printing can provide accurate control over the scaffold architecture. Direct ink writing can produce grid-like scaffolds with specific pore channel sizes. We have previously shown that hBM-MSCs cultured with chondrogenic differentiation medium (CDM) on these 3D printed SiO_2/PTHF/PCL-diCOOH hybrid scaffolds, of certain channel size, under normoxic conditions, differentiated down to the chondrogenic lineage [18]. SOX9, collagen type II, aggrecan and glucosaminoglycan production was high for the cells with round morphology cultured in the scaffolds with ~250 μm channel size; whereas, in the scaffolds with larger ~500 μm channels, the cells seemed to attach to the channel walls and become fibroblastic, producing mainly a collagen type I matrix [18]. Similar results were seen for mouse ATDC5 chondrogenic cell line cultured in the SiO_2/PTHF/PCL--diCOOH hybrids [11] and silica/gelatin hybrid scaffolds [19]. All these *in vitro* cultures used CDM but there was some evidence that the material itself stimulated chondrogenesis, as in parallel experiments when the cells were cultured in scaffolds made solely of PCL (with similar pore architectures), the cells produced a lower amount of collagen type II and more collagen type I [11].

Here, we investigated the ability of the 3D printed SiO_2/PTHF/PCL-diCOOH hybrid scaffolds to promote hBM-MSC chondrogenesis *in vitro* under more clinically relevant hypoxic conditions, with or without chondrogenic supplements. Physiological hypoxia (2–5 % O_2) plays a role in both the formation and maintenance of cartilage [20–23]. When MSCs are cultured under hypoxic conditions, p38 MAPK is phosphorylated leading to the activation of the hypoxia-inducible factor (HIF)−1α pathway, triggering the expression of the master transcriptional regulator of chondrogenesis, *SOX9* [24], and upregulating its downstream targets [25], the ECM genes *COL2A1* and *ACAN* [22,23]. In this way, hypoxia drives chondrogenesis [20,21]. Concomitantly, hypoxia suppresses chondrocyte hypertrophy [26], by blocking HDAC4, Nkx3.2, and Smad6 activation that results in suppression of *RUNX2, COL10A1, MMP13* and *ALP* [27,28]. HIF-2α acts as a chondrogenic factor supporting *COL2A1* and *ACAN* expression in articular chondrocytes under hypoxic conditions [29]. The genes *EGLN*and *PGK1* are established targets of the HIF transcriptional complex [30,31] and are important in driving the transition to anaerobic metabolism. HIF-1α drives the transcription of *P4HA1*, which catalyses collagen type II hydroxylation [32]. An elevated *LOX* expression, which can be activated via HIF-1α, has been linked to osteoarthritis [33], whereas appropriate LOX-mediated collagen cross-linking contributes to ECM structure and tension integrity, and cartilage biomechanical properties [34]. A hypoxic environment is therefore important in driving chondrogenesis, sustaining the articular chondrocyte phenotype and enhancing chondrocyte secretion of ECM [22,23]. Furthermore, condensation of the mesenchyme in the limb bud involves close cell-cell interactions mediated by adhesion molecules, such as N-cadherin and N-CAM and initiates chondrogenesis in the developing growth plate [35]. In a similar way, pellet or micromass cultures are conducive to MSC chondrogenesis [36]. Likewise, the mechanical properties of biomaterials [37,38], transforming growth factor-β (TGFβ) and Wnt/β-catenin signalling [39] all induce the formation of aggregates *in vitro* [40], improving chondrogenic lineage specification [37,40].

To advance this medical device towards functional validation in preclinical trials, a robust protocol for the sterilisation which would not change 3D printed SiO_2/PTHF/PCL-diCOOH hybrid scaffolds properties needed to be established. Dry heat and steam sterilisation would deform and degrade the scaffold's porous structure. Ethylene oxide sterilisation is an established alternative for degradable polymers [41], however, a major drawback of its use is the technical and practical difficulty associated with the removal of the toxic ethylene oxide residues from polymers [42]. γ-irradiation can cause dose-dependent chemical changes in polymers [43] that impact the properties of the scaffolds [44,45], so in this study, we investigated its effects on the scaffold microstructure, chemical composition and mechanical properties.

Additionally, a critical step in the development of these scaffolds for tissue engineering applications is the evaluation of the *in vivo* systemic toxicity and immune response. The inherent scaffold cues, such as geometry, micro- and nano-topography, chemical and physical composition, and mechanical properties critically influence the cascade of events following the scaffold implantation [46–51]. Indeed, the type of inflammatory response to the implanted scaffold determines the regenerative outcome [46]. A normal inflammatory response to any implant begins with the spontaneous non-specific adsorption of proteins to the surface of the scaffold (Vroman Effect) that has been shown to immediately stimulate the recruitment of modest numbers of neutrophils and monocyte-derived macrophages to the vicinity of the implant. If this inflammatory response quickly resolves, the scaffold can integrate and can promote new tissue formation. In contrast, persistent inflammation with the formation of foreign body giant polynuclear cells and ultimately fibrosis is characteristic of classical foreign body response and leads to pathological damage and disintegration of the surrounding tissue [46,52,53]. This detrimental outcome compromises efficacy or even precludes the specific scaffold function and leads to host discomfort or pain. Therefore, we investigated the systemic and local inflammatory responses caused by 3D printed SiO_2/PTHF/PCL-diCOOH hybrid scaffolds implanted subcutaneously in immunocompetent Balb/c mice.

Materials and methods

Hybrid synthesis and scaffold printing

SiO_2/PTHF/PCL-diCOOH sol-gel hybrid ink was prepared as described previously [11]. The organic component was obtained through the conversion of PCL-diol (M_n = 530 Da) to dicarboxylic acid (PCL-diCOOH), and co-polymerisation of (3-glycidyloxypropyl)trimethoxysilane (GPTMS) and THF in the presence of boron trifluoride diethyletherate (BF_3•OEt_2). The silica precursor, tetraethyl orthosilicate (TEOS, 80 wt% with regards to PCL-diCOOH mass) was hydrolysed in deionised water with 1 M HCl, at a ratio of 1:3 %v/v with respect to water. When fully reacted, the TEOS sol was added dropwise to the organic precursor solution and stirred at room temperature for 30 min in a sealed container to form the hybrid sol. Stirring was continued without a lid to evaporate part of the residual THF and accelerate the gelation process. If present, bubbles were removed via an ultrasound bath in this phase. When a suitable viscosity was reached, the ink was transferred into a 3 mL Luer-lock plastic syringe and residual air was carefully removed. The syringe was stored in a freezer at −82 °C. The ink composition was termed Si80-CL [11].

Si80-CL ink was printed directly from the sol-gel by direct ink writing, as described previously [11] ("Robocaster", 3d Inks LLC, USA). 3D porous scaffolds were printed following an orthogonal grid-like pattern using the following printing parameters: conical nozzle with an internal diameter of 0.20 mm, strut spacing of 0.60 mm, speed of 10 mm s^{-1}, and z-spacing of 0.21 mm. Si80-CL scaffolds with nominal side dimensions of 10.8 mm and height of 4.2 or 7.14 mm were printed. Wet scaffolds were moved into Nalgene polymethylpentene (PMP) containers, sealed and placed at 40 °C for ageing (3 days) and drying (gradual loosening of the lid over 4–7 days). When fully dried, the

shrinkage led to final side dimensions of ~7–8 mm and a final thickness of ~2.5 or 5 mm. Scaffolds were immersed in deionised water for 10 s to remove reaction by-products.

For mechanical testing and *in vitro* experiments, scaffolds were cut with a razor blade to 5×5 ×5 mm^3 for mechanical testing and 5×5×2.5 mm^3 for *in vitro* testing. For *in vivo* experiments scaffolds were manually punched into a circular section of 5 mm in diameter, resulting in disc-shaped scaffolds (5 mm diameter, 2.5 mm thick).

Sterilisation and the effect of γ-irradiation dose on 3D printed hybrid scaffolds

3D printed SiO_2/PTHF/PCL-diCOOH hybrid scaffolds were transferred to glass vials (Supelco) and exposed to 25, 50, and 100 kGy γ-irradiation using a Gammacell 1000 (Best Theratronics Ltd., UK).

The mechanical, microstructural and chemical properties of the scaffolds were assessed after γ-irradiation, to determine the optimal dose for sterilisation. Unsterilised Si80-CL were used as control samples.

Possible variations in the inorganic/organic ratio of the hybrid scaffolds before and after γ-irradiation were assessed by thermal gravimetric analysis (TGA), as the weight loss measured during the test was due to the burning-out of the organic phase. Differential scanning calorimetry/thermal gravimetric analysis (DSC/TGA, Netzsch Jupiter STA 449C) was performed on ground powders (10–15 mg) in a platinum crucible in the temperature range 20–800 °C with a heating rate of 10 °C min^{-1} in an atmosphere of continuously flowing air.

Dynamic mechanical analysis (DMA) analysis was carried out using a Bose Electroforce Series III (TA Instruments), fitted with a 220 N load cell, at 3 frequencies (0.1–1–10 Hz). The tests were performed in displacement control and repeated in three different ranges of strain (ε_c): the displacement was set to (I) 1–5 %, (II) 5–9 % and (III) 9–13 % of the initial sample height, respectively ($n \geq 4$). The WinTest® DMA software allowed the calculation of the storage modulus (E') and loss modulus and loss tangent (E'' and tan(δ), respectively).

Scanning electron microscopy (SEM, JEOL 6010 LA, secondary electron imaging (SEI), 20 kV voltage, working distance between 13 and 20 mm) was applied to the top surface of the scaffolds coated with a 15 nm layer of gold. SEM images of the top surface of the scaffolds were analysed with ImageJ software to evaluate vertical channel size (*i.e.* the size of the pores in the direction of cell seeding) and strut size on the x–y plane ($n \geq 15$).

Fourier-transform infrared spectroscopy in attenuated total reflectance mode (ATR-FTIR) was carried out with a Thermo Scientific Nicolet iS10 FTIR equipped with Smart Golden Gate for Single-Reflection Diamond ATR Analysis with OMNIC software, using 64 scans at a resolution of 4 LP mm^{-1} in absorbance between the range 4000–400 cm^{-1}.

Mice

Balb/c females were purchased from Charles River UK Ltd. and were used for experiments between 7 and 10 weeks of age and randomly selected in two groups. Mice were housed under specific pathogen-free conditions and given food and water *ad libitum*. All procedures were conducted following the institutional guidelines and under the approval of our Home Office project license [granted under the Animals (Scientific Procedures) Act 1986]. All animals were kept at constant room temperature (~22 °C), humidity (~52 %) and under a controlled 12 h light/dark cycle. All animal procedures were carried out following the "3Rs" policy (Replacement, Reduction and Refinement).

Surgical procedure

Mice were given subcutaneously analgesic buprenorphine (Vetergesic®, Ceva) diluted to 0.05 mg/mL in 0.9 % saline solution, used at a dose of 1 μg/Kg. Anaesthesia was induced in a chamber with 5 % isoflurane (IsoFlo®, Abbot Laboratories) and oxygen (2 L/min) and maintained at 1–3 % isoflurane in oxygen (2 L/min) using a nose cone. Surgical procedures were performed using an aseptic technique throughout. A small dorsal area was shaved and cleaned by swabbing with 1 % w/v iodinated povidone (Videne antiseptic solution, Ecolab) in water for injections (Hameln Pharmaceuticals Ltd.). To implant the scaffold, a small incision (< 1 cm) was made using a sterile scalpel (Swann-Morton) on the central dorsal surface. Autoclaved blunt Adson forceps (WPI) were used to create a pocket in the subcutaneous space for each scaffold. One sterilised disc-shaped 3D printed SiO_2/PTHF/PCL-diCOOH hybrid scaffold was implanted into each mouse, ~1 cm apart from the skin incision. After implantation, each wound was closed with an autoclaved 9 mm surgical Reflex clip with clip applier (WPI). Sham surgery was performed in the control group. After surgery, mice were removed from anaesthesia and transferred to a recovery chamber at 37 °C. Mice were carefully monitored by animal care services and housed for 1 or 7 days ($n = 5$ mice for each group). The experiment was repeated twice for each time point.

Euthanasia and specimen harvest

24 h and 7 days post scaffold implantation, mice were euthanised by anaesthetic overdose (pentobarbitone sodium, 0.6–0.8 mg/kg, Animalcare) by intraperitoneal injection. Peripheral blood was collected with a sodium-heparin micro haematocrit capillary tube (Brand) at room temperature after severing the neck jugular vein. Collected blood was used for differential counts and ELISA, with processing details to follow. Then, the dorsal skin was shaved and carefully resected. Pictures were recorded after exposing the underskin in the surgery area and the area covering the scaffold. The clipped wound sites were avoided in the morphologic evaluation. Skin from the surgery area (sham), skin in contact with the scaffold and naïve skin (~1 cm^2) were excised.

Differential white blood cell count

Blood (100 μL/mouse) was incubated for 5 min with 3 mL red blood cells lysis buffer (155 mM ammonium chloride, 10 mM potassium hydrogen carbonate and 0.1 mM EDTA, pH 7.4 (all from VWR)), then neutralised with 7 mL of PBS and the cell pellet was recovered after centrifugation 2500 *g* for 5 min. The red blood cell lysis procedure was repeated twice.

Total cell counts were done with filtered 0.2 μm white cell counting fluid corresponding to 0.02 % (w/v) crystal violet solution (Sigma), and 0.04 % (v/v) acetic acid (VWR) in PBS.

Cell suspension (5×10^4 cells/100 μL) was deposited as a monolayer of cells on slides using Shandon Cytospin 3 cytocentrifuge at 400 rpm/4 min, fixed 5 min with methanol and air-dried. Then slides were stained with Shandon™ Kwik-Diff™ Stains (Fisher Scientific) following the manufacturer's instructions. Slides were coverslipped with DPX mounting medium (BDH). Neutrophils, lymph mononuclear cells and eosinophils were counted in 7–10 fields in random view under the Zeiss Axioskop microscope to complete a total of ~400 white blood cells, using a 20 × dry objective with a numerical aperture of 0.5.

ELISA

Blood was centrifuged at 16.3 *g* for 10 min. The serum was collected and frozen at −20 °C. Serum tumour necrosis factor-alpha (TNFα) levels were measured by ELISA (mouse uncoated TNFα ELISA, Life Technologies Ltd.) according to the manufacturer's protocol.

Histology

The excised specimens were fixed at 4 °C in 10 % neutral buffered formalin (Sigma) for 24 h. After paraffin wax embedding, 5 μm thick sections were dewaxed immersing twice for 5 min in Gentaclear (Genta Medical) and washed in tap water. Sections were then washed twice

with 100 %, 90 % and then 70 % Industrial Methylated Spirit (IMS, Fisher Scientific) and rinsed with tap water. For Hematoxylin-Eosin staining, sections were stained for 2 min with Harris Haematoxylin mercury-free (VWR), washed with tap water, and then differentiated using acid alcohol (1 % hydrochloric acid in 70 % IMS) for 2 min. After washing with water, sections were stained with 1 % Eosin (VWR) for 1 min and then rinsed with water. Sections were stained for Masson's Trichrome as previously described [54]. All sections were dehydrated with serious dilutions of IMS, washed three times for 5 min with Gentaclear, and finally coverslipped with DPX mounting medium.

Hematoxylin and eosin stain cell nuclei blue and cytosol pink. Masson's Trichrome stains nuclei dark brown to black and collagen blue. Colour micrographs were acquired using a Zeiss Axio Observer Inverted Widefield Microscope with an IC5 colour camera, and with a ZEN Blue pro software capable of tiling and stitching, using a 5 × air objective with a numerical aperture of 0.16 or 10 × air objective with a numerical aperture of 0.3.

To quantify the cell number infiltrated inside the scaffold, after defining the scaffold area using a region of interest (ROI) delineated at the scaffold-host tissue interface in Hematoxylin-Eosin images, the blue image obtained with the colour deconvolution tool was thresholded with the Yen method and the cell number (20–100 μm) within the scaffold area was calculated in ImageJ (4 sections/sample, 5 mice/group, the experiment was repeated twice).

To quantify collagen deposition inside the scaffold, after defining the scaffold area using a ROI delineated at the scaffold-host tissue interface in Masson's Trichrome images, the blue image obtained with the colour deconvolution tool, was thresholded with the Yen method and the number of collagen blue fibers (> 100 μm) within the scaffold area was calculated in ImageJ (2 sections/sample, 5 mice/group, the experiment was repeated twice). Results obtained for each mouse were averaged.

Sections were imaged to evaluate the presence of round/ovoid shape mononuclear cells, polymorphonuclear leukocytes, foreign body giant polynuclear cells (cells that were fused with the nuclei centrally placed and overlapped), scaffold encapsulation (avascular collagenous fibers oriented in parallel to the outer surface of the implants in contact with the normal host tissue) and blood vessels (with intact lumen structure with the presence of pink-red blood cells). Sections were imaged using a Leica DM 2500 with Leica DFC 300FX camera, using a 40 × air objective with a numerical aperture of 0.85. 12 systematic random sampling areas (327 × 245 μm/field) per section (2 sections/sample, 5 mice/group, the experiment was repeated twice), within the hypodermis below the panniculus carnosus muscle, for sham surgeries sections, or between the scaffold-host tissue interface and the panniculus carnosus muscle, for implanted scaffolds sections.

hBM-MSCs culture and seeding on 3D printed hybrid scaffolds

Human bone marrow-derived mesenchymal stem/stromal cells (hBM-MSCs; #PT-2501, Lonza) were expanded in alpha-modified Eagle's medium (αMEM, no nucleosides (Thermo Fisher Scientific)) with 10 % Fetal Bovine Serum (FBS, Gibco). hBM-MSCs were used before passage 5 and were tested and devoid of mycoplasma contamination before being used in each experiment.

3D printed SiO_2/PTHF/PCL-diCOOH hybrid scaffolds were immobilised in sterile polystyrene moulds (#C3983–50EA, Sigma) sealed with autoclaved high-vacuum silicone grease (#Z273554–1EA, Aldrich) and placed within 48-well suspension plates (Greiner Bio-One). Scaffolds were washed twice with αMEM and centrifuged at 310 *g* for 5 min to remove bubbles. Then scaffolds were kept at 37 °C in a humidified atmosphere of 5 % CO_2/95 % air for 15 min. hBM-MSCs were trypsinised at ~80 % confluency using 0.05 % Trypsin-EDTA (Thermo Fisher Scientific) and pelleted. Cells were resuspended in αMEM (250 μL at 2 × 10^6 cells/mL), seeded within each scaffold and allowed to anchor under standard culture conditions for 2.5 h, while shaking each 30 min, at 200 rpm for 5 min. Then, 900 μL of basal medium (BM) solution was added. Moulds were removed after 3 days, and cell-seeded scaffolds were transferred to a new 48-well suspension plate and cultured for 21 days with 1) BM under standard culture conditions (normoxia, 20 % O_2, routinely used in tissue culture incubators, actually non-physiological); or 2) BM under hypoxic conditions (5 % O_2); or 3) chondrogenic differentiation medium (CDM) under hypoxic conditions.

CDM consisted of High Glucose Dulbecco's Modified Eagle Medium (#D5671, Sigma) supplemented with 2 mM L-glutamine (Thermo Fisher Scientific), 100 nM dexamethasome (Sigma), 1 % insulin, transferrin, selenium solution (Thermo Fisher Scientific), 1 % antibiotic-antimycotic solution (Sigma), 50 μg/mL ascorbic acid-2-phosphate (Sigma), 40 μg/mL L-proline (Sigma) and 10 ng/mL TGF-β3 (Peprotech Inc.). BM consisted of αMEM, no nucleosides, supplemented with 10 % FBS and 1 % (v/v) antibiotic-antimycotic solution. Media were exchanged every 2 days.

hBM-MSCs viability within scaffolds

hBM-MSCs viability within scaffolds was confirmed by staining with a LIVE/DEAD® viability/cytotoxicity kit for mammalian cells (Molecular Probes) according to the manufacturer's instructions. Cell seeded-scaffolds were transferred into a μ-Slide 8 Well uncoated, polymer coverslip, hydrophobic, sterilised (Ibidi), incubated for 15 min in 1 μM calcein AM and 1 μM ethidium homodimer-1 in FluoroBrite™ DMEM (Gibco) with 10 % FBS and 1 % (v/v) antibiotic-antimycotic solution. Cell-seeded scaffolds were imaged on a Zeiss Axio Observer Inverted Widefield Microscope with a Hamamatsu Flash 4.0 fast camera, using a 5 × air objective with a numerical aperture of 0.16. Representative images are Z-projections of 10 Z-slices of 3.45 μm spacing obtained using Image J.

Gene expression analyses of hBM-MSC differentiation within scaffolds

Cell-seeded scaffolds were snap-frozen in liquid nitrogen and stored at −80 °C. RNA was isolated using QIAshredder, RNeasy mini kit and RNase-free DNase set according to the manufacturer's instructions (all from Qiagen). The RNA quality and concentration were assessed using Nanodrop ND-1000. RNA was reverse transcribed into cDNA as previously described [55] and stored at −20 °C. RT-qPCR was performed on an Applied Biosystems ViiA 7 real-time PCR (Thermo Fisher Scientific) using 384-Well PCR plates. Primer sequences used for gene expression analyses are shown in Supplementary Table 1. Each primer pair concentration was optimised to maximum efficiency. Reaction mixtures were prepared and run in triplicate with a 3-step cycle as previously described [55]. Water was used instead of cDNA as a control.

The ΔΔCQ method was used to quantify fold changes in the expression for each gene of interest (GOI) and normalised to the expression of undifferentiated/naïve hBM-MSCs (hBM-MSCs suspension before seeding on the scaffolds at day 0, set to 1), using *EEF1A1, RPL13A* [56,57] and *PPIA* [58] as the reference genes (RG): fold change in expression $= 2^{-\Delta\Delta Cq}$, $\Delta\Delta Cq = [(Cq_{GOI,t(21\ days)} - Cq_{RG,t(21\ days)}) - (Cq_{GOI,t(0)} - Cq_{RG,t(0)})]$.

Immunocytochemistry of hBM-MSCs cultured within 3D printed hybrid scaffolds

Cell-seeded scaffolds were fixed in 4 % (w/v) paraformaldehyde in phosphate-buffered saline (PBS, without calcium and magnesium) for 20 min, permeabilised with 0.1 % (v/v) Triton-X 100 in PBS for 10 min and blocked for 1 h with 10 % (v/v) horse serum in 0.15 % (w/v) glycine and 0.2 % (w/v) bovine serum albumin in PBS (all from Sigma). Samples were stained overnight at 4 °C with primary antibodies, washed trice and stained for 1 h at room temperature with secondary antibodies (Supplementary Table 2). After washing, nuclei were counterstained for 15 min at room temperature with 10 μg/mL Hoechst 33342, Trihydrochloride, Trihydrate (Thermo Fisher Scientific). After washing, stained

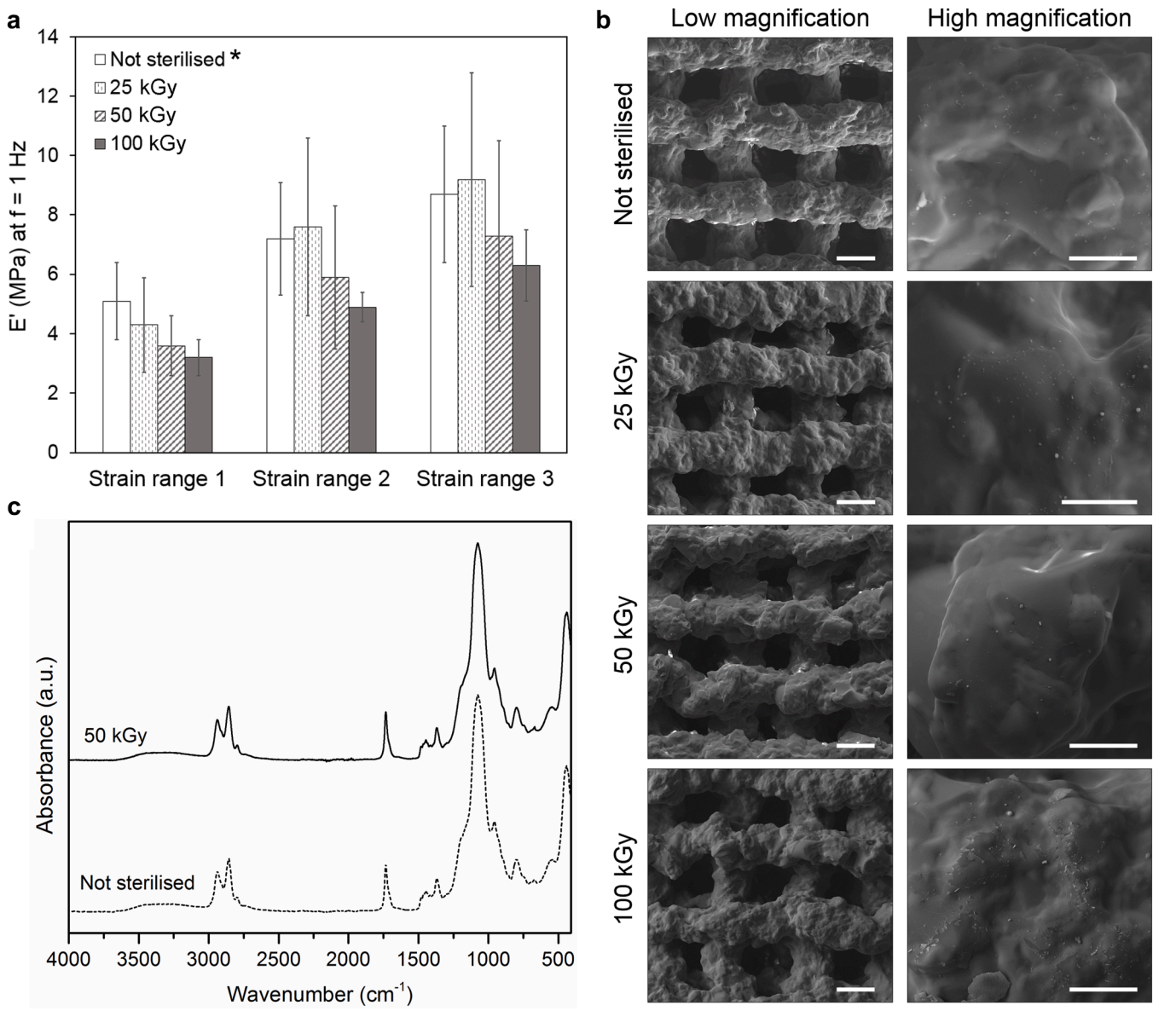

Fig. 1. γ-irradiation at 50 kGy efficiently sterilises 3D printed SiO_2/PTHF/PCL-diCOOH hybrid scaffolds without affecting their properties.
Characterisation of the hybrid scaffolds after γ-irradiation at 25, 50 and 100 kGy: a. mechanical properties evaluated by comparing the storage modulus (E') obtained via DMA at 1 Hz before and after sterilisation ($n \geq 4$). * "Strain range 1″ corresponds to 1–5 % for all samples; "Strain range 2″ corresponds to 5–9 % for all sterilised samples and 5–10 % for the control sample; "Strain range 3″ corresponds to 9–13 % for all sterilised samples and 10–15 % for the control sample; b. SEM representative micrographs of the top surface of 3D printed hybrid scaffolds before and after γ-irradiation with 25, 50, and 100 kGy; Scale bar is 200 μm at low magnification (70x) and 50 μm at high magnification (500x). c. ATR-FTIR spectra comparing hybrid scaffolds before and after γ-irradiation at 50 kGy.

samples were transferred to μ-Slide 8-Well and imaged in a Leica SP8 inverted confocal laser scanning microscope. Samples were then cut and the surface and interior sections of the cell-seeded scaffolds were imaged to confirm cells were distributed through the scaffold architecture. Detector gains were set to be constant among samples to facilitate comparison. Z-series with 1 μm Z-spacing were obtained using sequential acquisition and Kalman filter mode, 20 × dry objective with a numerical aperture of 0.75, and 2048 × 2048 pixel size.

Sox9, Aggrecan, collagen type II and collagen type X integrated density (arbitrary units) was calculated after thresholding with the Huang method in ImageJ and normalised by cell number calculated in the same volume. Representative images are 3D projections of 100 Z-slices of 1 μm obtained using ImageJ.

Statistical analyses

The number of mononuclear cells or collagen fibers inside each scaffold slice area are shown as scatter dot plots expressing the means ± standard deviations. Gene expression analyses and the normalised number of neutrophils in the blood are shown as column graphs with scatter dot plots showing the mean with standard deviation. Measurements of integrated density per cell (after removal of outliers with ROUT test $Q = 1$ %) are shown as scatter dot plots expressing the median. Statistical analyses were carried out using a non-parametric Kruskal-Wallis test followed by Dunn's multiple comparison test for multiple comparisons or a Mann-Whitney test (two-tailed) for comparisons between two groups. Statistical analyses were carried out using GraphPad Prism version 8 for Windows (GraphPad Software, USA). p values are indicated in figure captions.

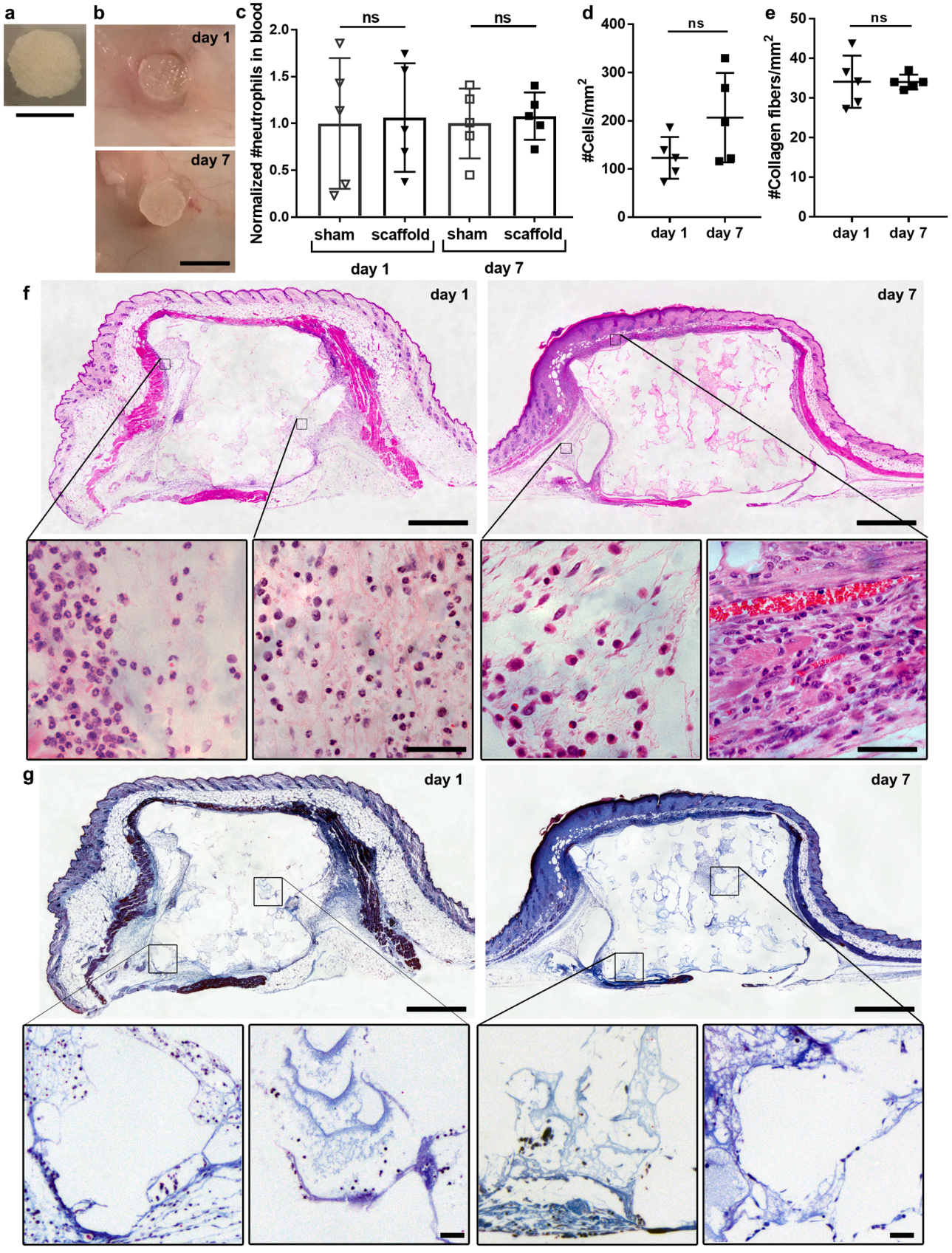

(caption on next page)

Fig. 2. 3D printed SiO_2/PTHF/PCL-diCOOH hybrid scaffolds subcutaneously implanted in Balb/c mice do not promote systemic inflammation and resolve quickly the local inflammatory response.
a. 3D printed SiO_2/PTHF/PCL-diCOOH hybrid scaffold. b. Representative macroscopic images of the explants 1 and 7 days after subcutaneous implantation of scaffolds in Balb/c mice ($n = 5$ mice per group). c. The normalised number of neutrophils in the blood 1 and 7 days after sham surgery and subcutaneous implantation of scaffolds in Balb/c mice ($n = 5$ mice per group, for one representative experiment). d. Number of infiltrated host mononuclear cells measured inside the scaffold (per mm^2). e. Number of collagen fibers per mm^2 of scaffold slice ($n = 5$ mice per group, for one representative experiment). f. Representative micrographs of hematoxylin and eosin stained slices (and insets) of the explants 1 and 7 days after subcutaneous implantation of scaffolds in Balb/c mice ($n = 5$ mice per group). g. Representative micrographs of Masson's trichrome stained slices (and insets) of the explants 1 and 7 days after subcutaneous implantation of 3D printed SiO_2/PTHF/PCL-diCOOH hybrid scaffolds in Balb/c mice ($n = 5$ mice per group). In c, d and e a Mann-Whitney test (two-tailed) was used to detect statistical significance (see Supplementary Table 3 for statistical analyses). Scale bars in a and b are 5 mm, f and g are 1 mm, and in insets are 50 μm.

Results

3D printed hybrid scaffolds properties are not changed by efficient sterilisation

In order to use 3D printed SiO_2/PTHF/PCL-diCOOH hybrid scaffolds as a medical device, a robust sterilisation protocol is required, that would eliminate any bioburden without affecting the mechanical, microstructural and chemical properties of the scaffolds. We, therefore, investigated the effect of using γ-irradiation, between 25 and 100 kGy following standard ISO 11137. We first determined that the 25 kGy dose was unsuitable, as it failed to prevent bacteria growth when scaffolds were subsequently kept in the basal medium under standard culture conditions for up to 7 days. In contrast, the 50 and 100 kGy doses eliminated the bioburden.

Post-sterilisation, we observed no significant variation in the inorganic/organic ratio of the hybrid by TGA: unsterilised Si80-CL scaffolds showed 74.8 wt.% organic content; post-sterilisation the organic content remained in the range of 74.8 % ± 0.3 %.

DMA showed very low E'' and tan(δ) values, confirming the elastic behaviour of the scaffolds, and their ability to recover the deformation in the investigated strain intervals. No differences were observed within the investigated range of frequencies (0.1 to 10 Hz). Hence E' values at 1 Hz were compared (Fig. 1a): when the dose increased from 25 to 100 kGy, a minimal decrease of the mean E' value and a narrowing of the standard deviation were observed, compared to the unsterilised control.

SEM imaging showed that the scaffold 3D grid-like architecture was not affected by the sterilisation (Fig. 1b at low magnification). The mean channel size ($n \geq 15$) was 213 ± 20 μm, for the scaffolds pre-sterilisation; 198 ± 41 μm after 25 kGy; 181 ± 44 μm after 50 kGy; and 205 ± 40 μm after 100 kGy. The mean strut size ($n \geq 15$) was 212 ± 33 μm, for the scaffolds pre-sterilisation; 223 ± 20 μm after 25 kGy; 227 ± 29 μm after 50 kGy; and 227 ± 24 μm after 100 kGy. Any variation in the channel size was within the error range of the not sterilised sample. This variation is due to the irregular surface of the scaffold struts, which is the result of the shrinkage inherent in the 3D printing directly from sol-gel. However, at higher magnification, we detected damage on the surface of the struts of the scaffolds sterilised at 100 kGy (Fig. 1b at high magnification). Finally, the ATR-FTIR spectra of the scaffolds sterilised at 50 kGy showed no significant differences from the scaffolds that were unsterilised, confirming that γ-irradiation had little to no effect on the chemical bonding within the hybrid network (Fig. 1c).

We conclude that 50 kGy γ-irradiation sterilised the scaffolds without affecting their microstructure, chemical composition and mechanical properties. This sterilisation protocol was, therefore, used for all the subsequent *in vivo* and *in vitro* experiments.

Subcutaneously implanted scaffolds trigger a rapid resolving local physiological reaction with infiltration of mononuclear cells

If the scaffolds are to become a medical device, it is important to determine whether they cause systemic toxicity and to understand the early inflammatory/immune response *in vivo*. Disc-shaped 3D printed SiO_2/PTHF/PCL-diCOOH hybrid scaffolds (Fig. 2a) were implanted subcutaneously in Balb/c mice for one week. The macroscopic evaluation showed no visible redness or darkening of the skin at the implantation site over the course of the study. Macroscopic images of the implanted scaffolds under the muscular layer of the dermis showed integration with the host tissue without evidence of infection, or toxic or undesirable side effects caused by the implanted scaffolds, suggesting good *in vivo* biocompatibility of the scaffolds (Fig. 2b). Scaffolds were surrounded by translucent connective tissue. Although the PCL component of the scaffolds is expected to degrade on contact with physiological fluids, the 3D printed hybrid scaffolds maintained native integrity *in vivo* over 7 days without obvious shape or structure loss. The scaffolds did not collapse due to the active movement of the mouse.

Implantation of the 3D printed hybrid scaffolds did not change the number of circulating neutrophils, as compared to the sham surgery at days 1 and 7 (Fig. 2c). The pro-inflammatory cytokine, TNFα was not detected in serum by ELISA at either time.

Histological analysis was carried out to evaluate any signs of leukocyte recruitment (1-day and 7-day time points; Fig. 2d, Fig. 2e, Fig. 2f, Fig. 2g and Supplementary Fig. 1). As expected, injury and implantation of foreign material led to a modest influx of leukocytes within the hypodermis, between the scaffold-host tissue interface and the panniculus carnosus muscle; and accumulation of adipose connective tissue (circular white areas (Fig. 2f)).

Within 1 week of implantation, a lower cell density was observed around the scaffold with the number of myeloid cells surrounding the scaffold decreased, denoting the resolution of the inflammatory response. No pathological reaction characterised by foreign body giant polynuclear cell formation was observed at the scaffold/tissue interface (Fig. 2f and g).

A randomly distributed population of host mononuclear cells was observed within the inner pores of the scaffolds, both in the periphery and centre of the scaffold by day 1 and day 7 (Fig. 2d,f,g).

A provisional matrix composed of loose sparse collagen fibers (blue staining in Masson's trichrome) surrounding and penetrating the scaffold architecture was observed similarly 1 or 7 days after implantation (Fig. 2e) reflecting the normal biofouling (spontaneous adsorption) observed when materials are in contact with physiological fluids. This result suggests potential neomatrix deposition within and throughout the scaffold. Within 1 week, the scaffolds were very thinly encapsulated, but with almost no collagenous fibers oriented in parallel to the outer surface of the implants, with occasional fibroblast-like cells (appearing spindle-shaped) intermingled with loose fibers, in the scaffold-host tissue interface (Fig. 2g). Areas of repaired muscle and few blood vessels and capillaries were detected surrounding the scaffolds in the dermis (Fig. 2f and g) confirming an early constructive remodelling response, typical of an active pro-healing environment, which suggests the scaffold integration within the skin. Sham surgery skin explants were similar to the naïve skin specimens in all histological features (Supplementary Fig. 1).

Our findings show that the interaction between the host immune system and the implanted scaffold elicited a local physiological reaction with infiltration of mononuclear cells responsible for scaffold-tissue integration and essential to promote the integration and healing of damaged tissue without any signs of a chronic inflammatory response.

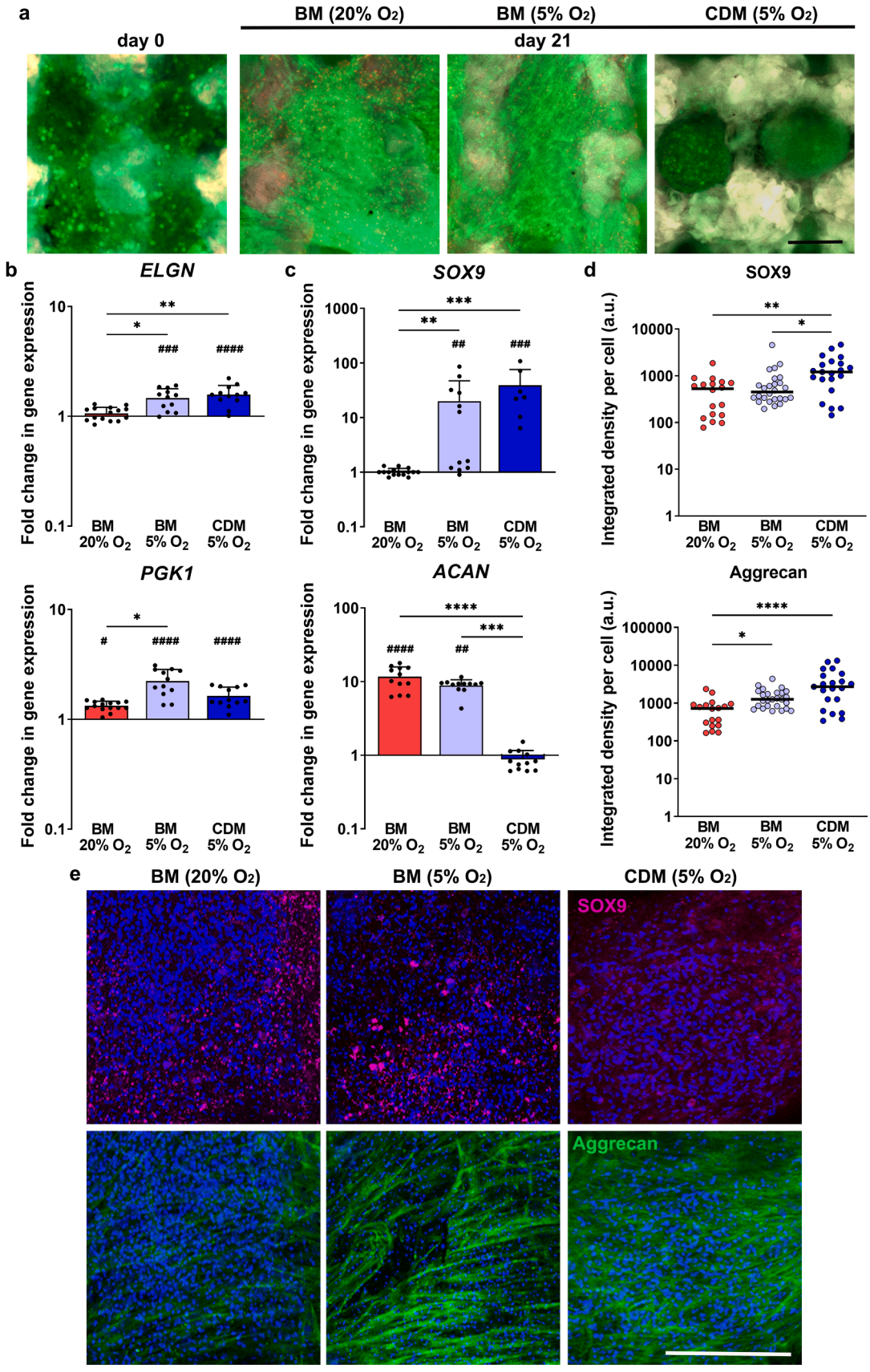

(caption on next page)

Fig. 3. Hypoxia activates HIF target genes and enhances hBM-MSC chondrogenesis within 3D printed SiO_2/PTHF/PCL-diCOOH hybrid scaffolds.
a. Representative micrographs of interior sections of the hBM-MSC-seeded 3D printed SiO_2/PTHF/PCL-diCOOH hybrid scaffolds ($n = 3$) stained with LIVE/DEAD® (green/red) at day 0 (Supplementary Figure 2) and after 21 days in culture under normoxic conditions (20 % O_2) with basal medium (BM) or hypoxic (5 % O_2) conditions, with BM or chondrogenic differentiation medium (CDM). The grid-like 3D porous structure of hybrid scaffolds is shown in grey. b. Gene expression analyses for HIF target genes (*ELGN* and *PGK1*) and c. Gene expression analyses for markers of chondrogenic differentiation (*SOX9* and *ACAN*) for hBM-MSCs cultured within 3D printed SiO_2/PTHF/PCL-diCOOH hybrid scaffolds for 21 days under normoxic conditions, in the presence of BM, or under hypoxic conditions in presence of BM or CDM, all normalised to undifferentiated/naïve hBM-MSCs (set to 1) ($n \geq 7$). d. Plots show the pixel intensity-based semi-quantification (integrated density of fluorescence signal showing the median as a black line) of SOX9 and aggrecan proteins produced per cell ($n \geq 15$ 3D projections). e. Representative micrographs of interior sections of the hBM-MSC-seeded scaffolds stained for SOX9 (magenta) and aggrecan (green) with nuclei counterstained with Hoechst (blue), after 21 days in culture under the normoxic conditions with BM, or hypoxic conditions with BM or CDM. In a and e scale bars are 200 μm. In b and c plots show means + s.d. In d plot shows the median. In b, c, and d a Kruskal-Wallis and Dunn's multiple comparison test was used to detect statistical significance: $^{*}p < 0.05$, $^{**}p < 0.01$, $^{***}p < 0.001$, $^{****}p < 0.0001$ for comparisons between groups, or $^{\#}p < 0.05$, $^{\#\#}p < 0.01$, $^{\#\#\#}p < 0.001$, $^{\#\#\#\#}p < 0.0001$ for comparisons with undifferentiated/naïve hBM-MSCs (see Supplementary Table 4 for statistical analyses).

3D printed hybrid scaffolds promote hBM-MSC chondrogenesis and hypoxia enhances articular cartilage-like matrix formation

The sterilised SiO_2/PTHF/PCL-diCOOH hybrid scaffolds were seeded with hBM-MSC and cultured under normoxic conditions in BM or hypoxic conditions in either BM or CDM for 21 days. The hBM-MSC-seed scaffolds were stained with LIVE/DEAD® to determine cell viability. hBM-MSCs were found to form a dense cell layer over and through the scaffold architecture on day 0 (Fig. 3a, Supplementary Figure 2). The LIVE/DEAD® images showed that the cells infiltrated the interconnected pores within the scaffold's interior, with the majority of the cells remaining viable (green) after 21 days (Fig. 3a).

We first sought to verify that the HIF pathway is activated when hBM-MSCs seeded within the SiO_2/PTHF/PCL-diCOOH hybrid scaffolds are cultured under hypoxic conditions. As shown in Fig. 3b, increased expression of *EGLN* and *PGK1* (targets of the HIF transcriptional complex) was observed when hBM-MSCs were cultured within the scaffolds under hypoxic conditions, irrespective of the composition of the media. This result is consistent with the hypothesis that hBM-MSCs cultured within 3D printed hybrid scaffolds respond to hypoxia by activating HIF. *PGK1* was also significantly upregulated when hBM-MSC-seeded scaffolds were cultured under the normoxic conditions with BM in comparison with undifferentiated/naïve hBM-MSCs control.

The chondrogenic induction of hBM-MSCs seeded within the 3D printed SiO_2/PTHF/PCL-diCOOH hybrid scaffolds was evaluated by quantifying the mRNA (Fig. 3c) and protein levels (Fig. 3d - quantification via image analysis; Fig. 3e - representative images) of the chondrogenic-related markers, *SOX9* (the master transcriptional regulator of chondrogenesis) and *ACAN* (the most abundant cartilage-specific proteoglycan, aggrecan), after 21 days in culture. SOX9 is required in all steps of chondrocyte differentiation, even preventing the conversion of proliferating chondrocytes into hypertrophic chondrocytes. Here, under hypoxic conditions, the *SOX9* gene was expressed at high levels irrespective of the culture medium type, while SOX9 protein was higher with CDM compared to BM. In BM, under normoxia, *SOX9* expression was similar to that of undifferentiated/naïve hBM-MSCs. SOX9 protein levels were significantly higher when hBM-MSCs were cultured within scaffolds under hypoxic conditions with CDM, compared to BM under normoxic or hypoxic conditions. As SOX9 protein was expressed at 21 days for hBM-MSCs cultured within scaffolds under the normoxic conditions in BM, the *SOX9* gene was likely turned on transiently prior to 21 days. Under hypoxic conditions, without chondrogenic supplements, *SOX9* gene expression is sustained at day 21, with CDM increasing both the expression of the gene and the protein production.

Upregulation of *ACAN* gene expression occurs in chondrogenesis, driving aggrecan production, which, once produced, forms part of the ECM. A*CAN* expression was significantly increased when the cell-seeded scaffolds were cultured for 21 days under normoxic and hypoxic conditions in BM. However, levels of aggrecan protein were higher in the cells cultured under hypoxia, compared to normoxic conditions. The highest level of aggrecan protein was observed in cells cultured under hypoxic conditions in CDM, while *ACAN* gene expression in these cells was similar to undifferentiated/naïve hBM-MSCs, suggesting that by 21 days it had been turned down, following the large production of protein.

The relative mRNA and protein levels of *COL2A1*, a marker of articular cartilage, and *COL10A1, a* marker of hypertrophic cartilage were evaluated. The expression of *COL2A1* despite heterogenous was significantly increased when hBM-MSC-seeded scaffolds were cultured for 21 days under normoxic and hypoxic conditions (Fig. 4a). The diverse *COL10A1* expression was not significantly different to undifferentiated/naïve hBM-MSCs in all culture conditions (Fig. 4a). The ratio of expression of *COL2A1* to *COL10A1* showed that *COL2A1* was dominantly expressed in all culture conditions (Fig. 4a) and significantly higher when CDM was combined with hypoxia. At the protein level, similar levels of collagen type II and collagen type X produced per cell were observed in all culture conditions (Fig. 4b - quantification via image analysis; Fig. 4c - representative images).

Suitable post-translational modifications of secreted collagen by enzymes encoded by *P4HA1* and *LOX* are required and are therefore typical of the articular cartilage phenotype. We observed upregulation of *P4HA1* in all culture conditions (Fig. 5a). *LOX* transcript levels were similar to the undifferentiated/naïve control in all conditions (Fig. 5a). To investigate whether the 3D printed SiO_2/PTHF/PCL-diCOOH hybrid scaffolds could also direct hBM-MSCs towards osteogenesis or hypertrophy, we carried out further gene expression analysis. *RUNX2*, a key regulator of osteogenesis, also expressed in hypertrophy, and *BGLAP,* another marker of osteogenesis, were not significantly upregulated under any of the tested conditions (Fig. 5b). *COL1A1,* which is highly expressed in fibrocartilage and bone matrix, was significantly downregulated when hBM-MSC-seeded scaffolds were cultured under the hypoxic conditions with BM (Fig. 5b). *VEGFA,* expressed by hypertrophic chondrocytes, was significantly downregulated when hBM-MSC-seeded scaffolds were cultured with CDM in hypoxia (Fig. 5b).

Importantly, the ratios of expression of *SOX9* to *RUNX2* (Fig. 5c) and *COL2A1* to *COL1A1* (Fig. 5d) denoted a significant trend towards chondrogenesis in hBM-MSC-seeded scaffolds cultured under hypoxic conditions that was much less pronounced when cultured in normoxia in BM. *MMP13*, a marker of hypertrophic differentiation and osteoarthritis-associated, was downregulated under hypoxic conditions in BM, consistent with the hypoxia's inhibitory role on chondrocyte hypertrophy. In the other conditions, *MMP13* was expressed in similar levels to undifferentiated/naïve control (Fig. 5e). Overall, these data suggest that hypoxia enhanced hBM-MSC differentiation towards articular chondrocyte-like genotype and phenotype.

Discussion

Here, we show that 3D printed SiO_2/PTHF/PCL-diCOOH hybrid scaffolds can be efficiently sterilised with 50 kGy γ-irradiation without affecting scaffold microstructure, chemical composition and mechanical properties. The *in vivo* experiments showed that the sterilised 3D printed SiO_2/PTHF/PCL-diCOOH hybrid scaffolds did not cause a systemic inflammatory reaction when subcutaneously implanted in Balb/c mice

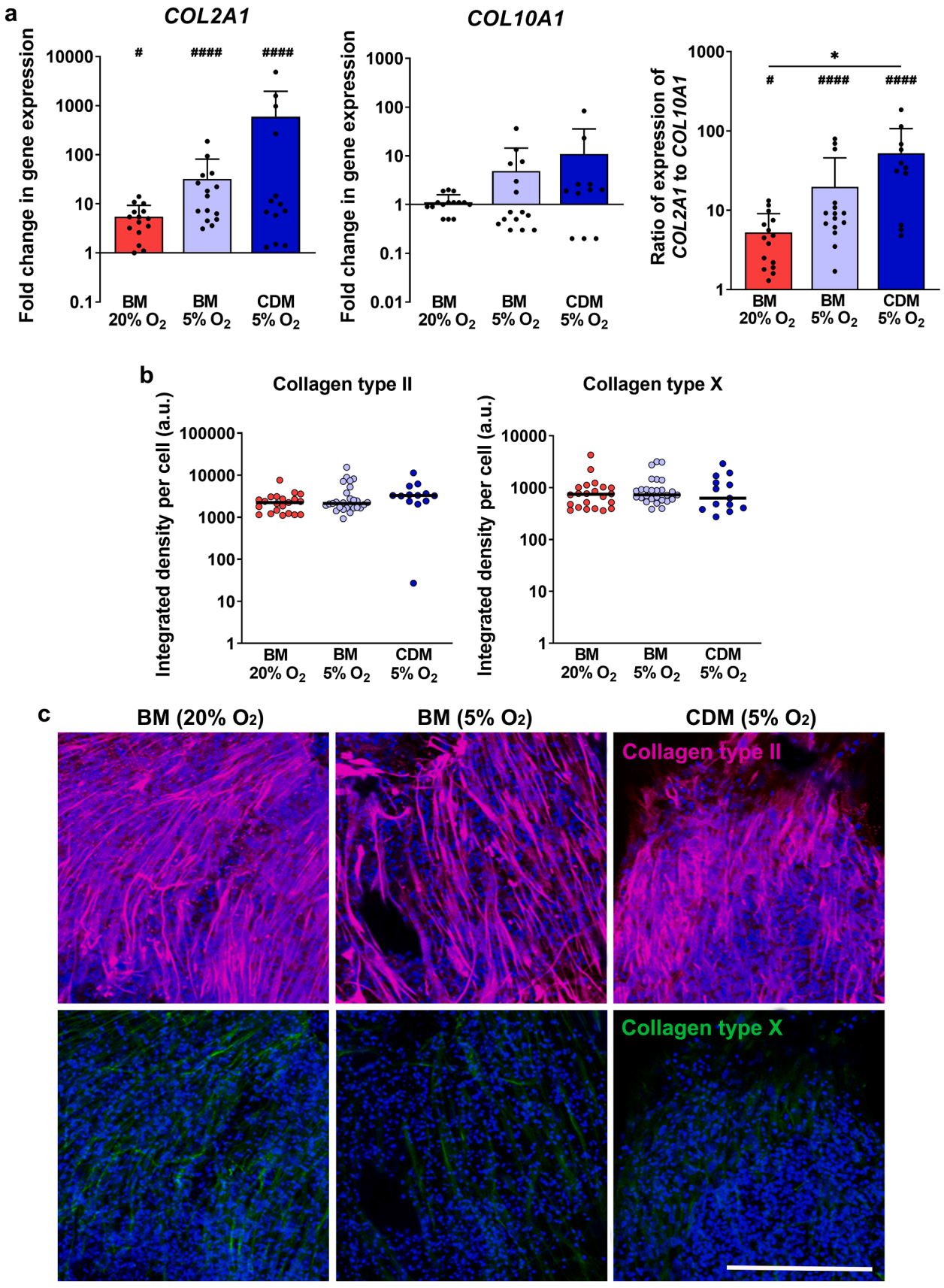

(caption on next page)

Fig. 4. Culture of hBM-MSC-seeded scaffolds under the hypoxic conditions with chondrogenic differentiation medium enhances hBM-MSC differentiation towards an articular chondrocyte-like phenotype.
a. Gene expression analyses for *COL2A1* (a marker of articular cartilage), *COL10A1* (a marker of hypertrophic cartilage), normalised to undifferentiated/naïve hBM-MSCs (set to 1) and ratio of the gene expression of *COL2A1* to *COL10A1* for hBM-MSCs within 3D printed SiO_2/PTHF/PCL-diCOOH hybrid scaffolds ($n \geq 10$, means + s.d). b. Plots show the pixel intensity-based semi-quantification (integrated density of fluorescence signal showing the median as a black line) of collagen type II and collagen type X produced per cell ($n \geq 13$ 3D projections). c. Representative micrographs of interior sections of the hBM-MSC-seeded scaffolds stained for collagen type II (magenta) and collagen type X (green) with nuclei counterstained with Hoechst (blue) after 21 days in culture under normoxic conditions (20 % O_2) with basal medium (BM), or hypoxic (5 % O_2) conditions with BM or chondrogenic differentiation medium (CDM). The scale bar is 200 μm. In a and b a Kruskal-Wallis and Dunn's multiple comparison test was used to detect statistical significance: $^{*}p < 0.05$ for comparisons between groups, or $^{\#}p < 0.05$, $^{\#\#\#\#}p < 0.0001$ for comparisons with undifferentiated hBM-MSCs (see Supplementary Table 5 for statistical analyses).

over one week. While initial recruitment of leukocytes was observed around the scaffold after 24 h, this had reduced by day 7. Further after one week, there were no foreign body giant polynuclear cells at the scaffold/tissue interface, which instead was surrounded by loose collagen fibers; and was devoid of features to suggest the formation of the high-density, thick, highly organised collagen fibrotic capsule. Overall this suggests that the local inflammatory response caused by 3D printed SiO_2/PTHF/PCL-diCOOH hybrid scaffolds resolves rather than leading towards chronic inflammation. This is an important finding since other biomaterials, including PCL, have been reported to stimulate a foreign body response when subcutaneously implanted [46–49], limiting their use in tissue engineering. The *in vivo* data also confirms the effective sterilisation of the scaffolds by γ-irradiation.

We show that 3D printed SiO_2/PTHF/PCL-diCOOH hybrid scaffolds support hBM-MSCs attachment, viability and chondrogenesis over 21 days in culture under normoxic or hypoxic conditions. Hypoxia can direct chondrogenesis in hBM-MSC-seeded biomaterials with distinct efficiencies and outcomes [37,59,60]. We show that the chondrogenesis of hBM-MSCs seeded within the SiO_2/PTHF/PCL-diCOOH hybrid scaffolds was enhanced under hypoxic conditions, even without chondrogenic supplements, with significant upregulation in chondrogenic genes (*SOX9*, *COL2A1*, *ACAN*) and a concomitant increased articular cartilage-specific matrix deposition as compared to hBM-MSCs cultured under the normoxic conditions. Gradients of expression in the markers of chondrogenesis are expectable *in vitro*, similar to the sequence of events observed during native chondrogenesis [61]. The ratios of expression of *SOX9* to *RUNX2, COL2A1* to *COL1A1* and *COL2A1* to *COL10A1* show that hBM-MSCs within these scaffolds responded to hypoxia to a similar degree, even in the absence of CDM. Still, the combined effect of low oxygen tension and chemical induction was more conducive for a cartilage-like matrix formation, with higher production of SOX9 and aggrecan within 21 days. However, following 21 days in culture with CDM in hypoxia, the *ACAN* gene was expressed at a similar level as the undifferentiated control. While the *ACAN* gene is expressed by undifferentiated MSCs [62,63], its expression is significantly upregulated during chodroprogenitor differentiation into chondrocytes [61,64] and continues during terminal differentiation [61,64]. Our results suggest that the *ACAN* gene was upregulated before day 21, leading to the high production of aggrecan protein that we evaluated by immunocytochemistry. This is in line with the other results we show, as chondrocytes are not becoming hypertrophic. *VEGFA,* a critical regulator in physiological angiogenesis and osteogenesis [65], also secreted by hypertrophic chondrocytes [66], was significantly downregulated when hBM-MSC-seeded scaffolds were cultured with CDM in hypoxia. In contrast to normoxic culture, hypoxia significantly downregulated the expression of *COL1A1* and the hypertrophic gene *MMP13*, while the expression of *COL10A1* was similar to the undifferentiated/naïve control. Immunocytochemistry results suggest that hypoxia does not completely suppress collagen type X protein production, which is in agreement with the observations of others [67–69].

Remarkably, under normoxia and in BM, hBM-MSCs seeded within the scaffolds produced high levels of SOX9, aggrecan and collagen type II proteins, as shown by immunocytochemistry, suggesting that the scaffold structure and its physico-chemical properties promote chondrogenesis. The dense cell distribution inside the grid structure of the 3D printed SiO_2/PTHF/PCL-diCOOH hybrid induced cell-cell interactions and might have governed oxygen gradients under normoxia creating local hypoxia. Others have suggested that a physioxic region might occur in the central regions of pellets or scaffolds, producing a greater amount of glycosaminoglycan and collagen type II [70,71]. This may also explain the increase in the expression of *PGK1* and *P4HA1*, targets of the HIF transcriptional complex [30,31], that we observed in this culture condition, suggesting that cell organization within these scaffolds mediated, at least in part, a hypoxic local environment inducive of chondrogenesis. hBM-MSC-seeded scaffolds cultured in BM under normoxia for 21 days showed that the *SOX9* gene expression returned to the baseline, with low expression of *COL2A1*, and high expression of *ACAN*. These results may suggest that chondrocytes are turning hypertrophic as it is known that the *SOX9* gene is turned off in hypertrophic chondrocytes, while low levels of *Col2A1* are still expressed, and the *ACAN* expression, which is switched on during chondrogenic differentiation, continues during hypertrophy [72]. However, we show that *RUNX2* [27,28], *COL10A1* [73] and *MMP13* [74,75], which are typical markers of matrix-mineralizing terminal hypertrophic chondrocytes [72], were expressed at similar levels as in undifferentiated/naïve control, which implies cells are not hypertrophic.

Overall, the *in vitro* data show that the scaffolds drive chondrogenesis of hBM-MSCs, which is enhanced under physiological hypoxia. This is important as it suggests that implantation of this 3D printed hybrid scaffold at sites of cartilage injury, where hypoxic condition prevails, has great potential to drive the formation of new cartilage. For accelerating clinical translation, the next preclinical step for functional validation will be confirming the efficacy of these scaffolds in a cartilage defect in a large animal model.

Conclusions

3D printed SiO_2/PTHF/PCL-diCOOH hybrid scaffolds were successfully sterilised by γ-irradiation. 3D printed SiO_2/PTHF/PCL-diCOOH hybrid scaffolds maintained their structure when subcutaneously implanted in mice, showed *in vivo* biocompatibility and a resolving mild local inflammatory response. Following hBM-MSCs culture within the scaffolds (~250 μm pore channels), the hBM-MSCs differentiated towards the chondrogenic lineage even in the absence of CDM, as shown by gene expression and protein deposition analyses. The chondrogenesis within these scaffolds was enhanced under hypoxic conditions, with high aggrecan production. Taken together these results suggest that the hypoxic conditions of endogenous cartilage would be optimal to drive chondrogenesis within these scaffolds.

The *in vivo* biocompatibility and *in vitro* chondrogenic differentiation of hBM-MSCs indicate that 3D printed SiO_2/PTHF/PCL-diCOOH hybrid scaffolds are promising medical devices for cartilage regeneration.

CRediT authorship contribution statement

Silvia A. Ferreira: Conceptualization, Data curation, Formal analysis, Investigation, Methodology, Project administration, Resources, Validation, Visualization, Writing – original draft, Writing – review & editing. **Francesca Tallia:** Conceptualization, Data curation, Formal analysis, Investigation, Methodology, Validation, Writing – original

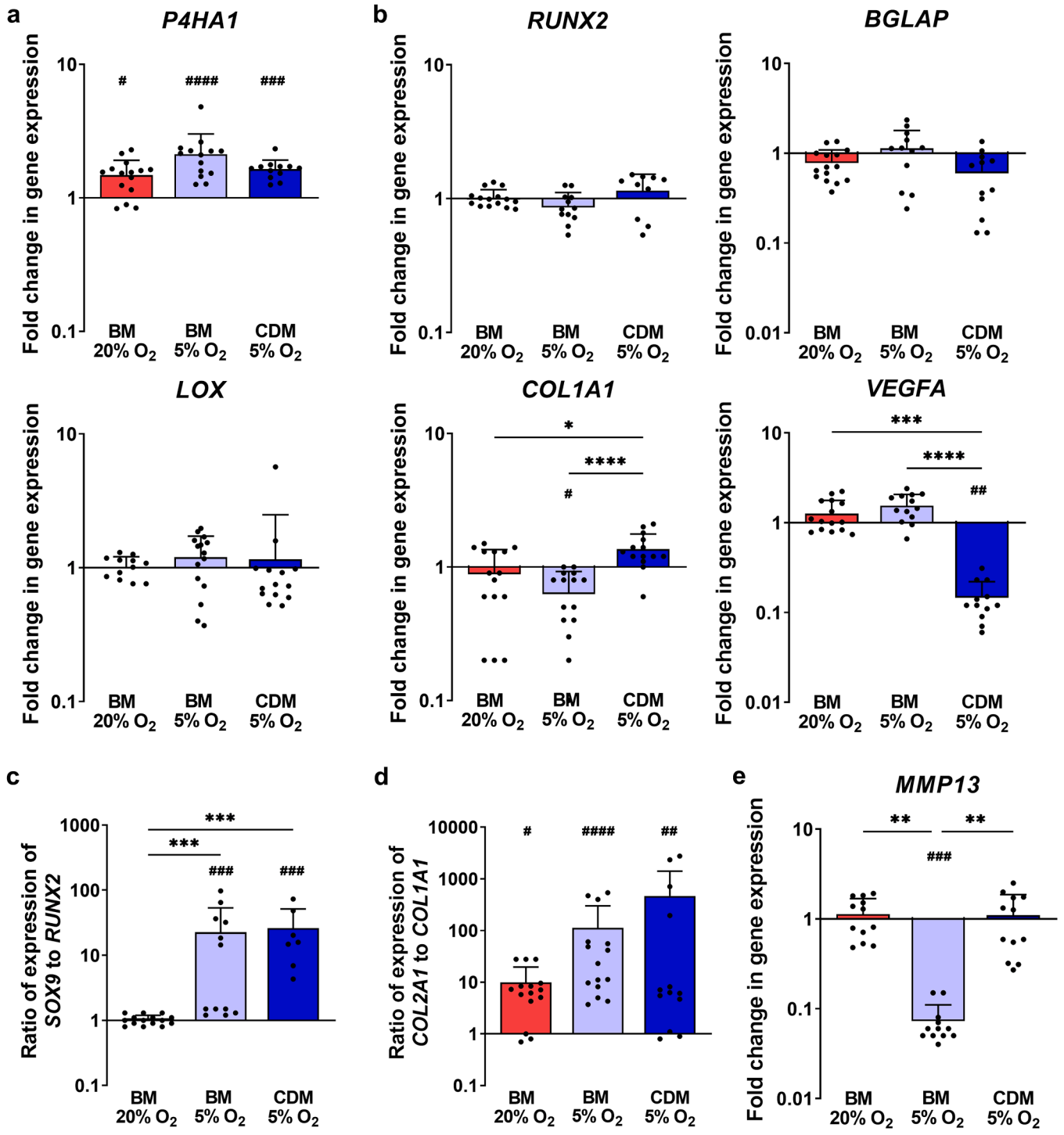

Fig. 5. Culture of hBM-MSCs within scaffolds precludes osteogenic and hypertrophic transcriptional profiles.
a. Gene expression analyses for *P4HA1* and *LOX* that encode for enzymes responsible for post-translational modifications of secreted collagen in articular cartilage. b. Gene expression analyses for hypertrophic/osteoblastic differentiation markers (*RUNX2, BGLAP, COL1A1, VEGFA*). c. Ratios of expression of *SOX9* to *RUNX2* and d. *COL2A1 to COL1A1*. e. Gene expression analyses for *MMP13* (a marker of hypertrophic cartilage) for hBM-MSCs within 3D printed SiO_2/PTHF/PCL-diCOOH hybrid scaffolds after 21 days in culture under normoxic conditions (20 % O_2) with basal medium (BM) or hypoxic conditions (5 % O_2) with BM or chondrogenic differentiation medium (CDM). In a, b, c, d and e expression levels (mean + s.d.) are shown as fold change normalised to expression in undifferentiated/naïve hBM-MSCs (set to 1) ($n \geq 8$). A Kruskal-Wallis and Dunn's multiple comparison test was used to detect statistical significance: $^{*}p < 0.05$, $^{**}p < 0.01$, $^{***}p < 0.001$, $^{****}p < 0.0001$ for comparisons between groups, or $^{\#}p < 0.05$, $^{\#\#}p < 0.01$, $^{\#\#\#}p < 0.001$, $^{\#\#\#\#}p < 0.0001$ for comparisons with undifferentiated/naïve hBM-MSCs (see Supplementary Table 6 for statistical analyses).

draft, Writing – review & editing, Visualization. **Agathe Heyraud:** Investigation, Methodology, Writing – original draft, Writing – review & editing. **Simone A. Walker:** Investigation, Methodology, Writing – original draft, Writing – review & editing, Validation. **Christoph Salzlechner:** Writing – original draft, Writing – review & editing, Resources. **Julian R. Jones:** Conceptualization, Funding acquisition, Project administration, Supervision, Writing – original draft, Writing – review & editing, Validation. **Sara M. Rankin:** Conceptualization, Funding acquisition, Supervision, Writing – original draft, Writing – review & editing.

Declaration of competing interest

The authors declare the following financial interests/personal relationships which may be considered as potential competing interests:

Tallia, F., Jones, J. R., Young, G., Cipolla, L., Russo, L., has patent "Hybrid materials and process for production thereof" WO2017168168. Issued to No commercial relationship. No license.

Acknowledgements

Authors acknowledge funding provided by EPSRC grant EP/N025059/1 and Lorraine Lawrence for preparation and staining of the histology slides. Authors acknowledge support and training provided by Dr Andreas Bruckbauer, Dr David Gaboriau and Stephen Rothery from the Facility for Imaging by Light Microscopy (FILM) at Imperial College London, which is part supported by funding from the Wellcome Trust (grant 104931/Z/14/Z) and BBSRC (grant BB/L015129/1).

Author contributions

S.A.F., F.T., A.H. developed experimental protocols, designed the experiments, conducted experiments, analysed and interpreted the data. S.W. conducted the animal surgeries, contributed to experimental design and interpretation. C.S. sterilised the 3D printed SiO_2/PTHF/PCL-diCOOH hybrid scaffolds. S.M.R. and J.R.J. obtained funding, initiated and supervised the project. All authors wrote the manuscript, revised and approved the manuscript.

Data availability

The authors declare that all data supporting the findings of this study are available within the article and its supplementary information files.

Data access statement

Raw data is available on request from rdm-enquiries@imperial.ac.uk.

Supplementary materials

Supplementary material associated with this article can be found, in the online version, at doi:10.1016/j.bbiosy.2024.100087.

References

[1] Zelinka A, Roelofs AJ, Kandel RA, De Bari C. Cellular therapy and tissue engineering for cartilage repair. Osteoarthr Cartil 2022;30:1547–60. https://doi.org/10.1016/j.joca.2022.07.012.
[2] Zhao X, Shah D, Gandhi K, Wei W, Dwibedi N, Webster L, Sambamoorthi U. Clinical, humanistic, and economic burden of osteoarthritis among noninstitutionalized adults in the United States. Osteoarthr Cartil 2019;27:1618–26. https://doi.org/10.1016/j.joca.2019.07.002.
[3] Moran CJ, Pascual-Garrido C, Chubinskaya S, Potter HG, Warren RF, Cole BJ, Rodeo SA. Restoration of articular cartilage. J Bone Joint Surg 2014;96:336–44. https://doi.org/10.2106/jbjs.L.01329.
[4] Kreuz PC, Steinwachs MR, Erggelet C, Krause SJ, Konrad G, Uhl M, Südkamp N. Results after microfracture of full-thickness chondral defects in different compartments in the knee. Osteoarthr Cartil 2006;14:1119–25. https://doi.org/10.1016/j.joca.2006.05.003.
[5] Benthien JP, Behrens P. The treatment of chondral and osteochondral defects of the knee with autologous matrix-induced chondrogenesis (AMIC): method description and recent developments. Knee Surg Sports Traumatol Arthrosc 2011;19:1316–9. https://doi.org/10.1007/s00167-010-1356-1.
[6] Gille J, Schuseil E, Wimmer J, Gellissen J, Schulz AP, Behrens P. Mid-term results of autologous matrix-induced chondrogenesis for treatment of focal cartilage defects in the knee. Knee Surg Sports Traumatol Arthrosc 2010;18:1456–64. https://doi.org/10.1007/s00167-010-1042-3.
[7] Schagemann J, Behrens P, Paech A, Riepenhof H, Kienast B, Mittelstadt H, Gille J. Mid-term outcome of arthroscopic AMIC for the treatment of articular cartilage defects in the knee joint is equivalent to mini-open procedures. Arch Orthop Trauma Surg 2018;138:819–25. https://doi.org/10.1007/s00402-018-2887-z.
[8] Kwan H, Chisari E, Khan WS. Cell-free scaffolds as a monotherapy for focal chondral knee defects. Materials 2020;13:306. https://doi.org/10.3390/ma13020306.
[9] Koh YG, Lee JA, Kim YS, Lee HY, Kim HJ, Kang KT. Optimal mechanical properties of a scaffold for cartilage regeneration using finite element analysis. J Tissue Eng 2019;10:1–10. https://doi.org/10.1177/2041731419832133.
[10] Setayeshmehr M, Esfandiari E, Rafieinia M, Hashemibeni B, Taheri-Kafrani A, Samadikuchaksaraei A, Kaplan DL, Moroni L, Joghataei MT. Hybrid and composite scaffolds based on extracellular matrices for cartilage tissue engineering. Tissue Eng Part B 2019;25:202–24. https://doi.org/10.1089/ten.teb.2018.0245.
[11] Tallia F, Russo L, Li S, Orrin ALH, Shi X, Chen S, Steele JAM, Meille S, Chevalier J, Lee PD, Stevens MM, Cipolla L, Jones JR. Bouncing and 3D printable hybrids with self-healing properties. Mater Horiz 2018;5:849. https://doi.org/10.1039/C8MH00027A.
[12] Jones JR. Review of bioactive glass: from Hench to hybrids. Acta Biomater 2013;9:4457–86. https://doi.org/10.1016/j.actbio.2012.08.023.
[13] Mahony O, Tsigkou O, Ionescu C, Minelli C, Ling L, Hanly R, Smith ME, Stevens MM, Jones JR. Silica-gelatin hybrids with tailorable degradation and mechanical properties for tissue regeneration. Adv Funct Mater 2010;20:3835–45. https://doi.org/10.1002/adfm.201000838.
[14] Mahony O, Yue S, Turdean-Ionescu C, Hanna JV, Smith ME, Lee PD, Jones JR. Silica-gelatin hybrids for tissue regeneration: inter-relationships between the process variables. J Solgel Sci Technol 2014;69:288–98. https://doi.org/10.1007/s10971-013-3214-3.
[15] Poologasundarampillai G, Yu B, Tsigkou O, Valliant EM, Yue S, Lee PD, Hamilton RW, Stevens MM, Kasuga T, Jones JR. Bioactive silica–poly(g-glutamic acid) hybrids for bone regeneration: effect of covalent coupling on dissolution and mechanical properties and fabrication of porous scaffolds. Soft Matter 2012;8:4822–32. https://doi.org/10.1039/c2sm00033d.
[16] Camarero-Espinosa S, Rothen-Rutishauser B, Foster EJ, Weder C. Articular cartilage: from formation to tissue engineering. Biomater Sci 2016;4:734–67. https://doi.org/10.1039/c6bm00068a.
[17] Vunjak-Novakovic G, Obradovic B, Martin I, Bursac PM, Langer R, Freed LE. Dynamic cell seeding of polymer scaffolds for cartilage tissue engineering. Biotechnol Prog 1998;14:193–202. https://doi.org/10.1021/bp970120j.
[18] Li SW, Tallia F, Mohammed AA, Stevens MM, Jones JR. Scaffold channel size influences stem cell differentiation pathway in 3-D printed silica hybrid scaffolds for cartilage regeneration. Biomater Sci 2020;8:4458–66. https://doi.org/10.1039/c9bm01829h.
[19] Nelson M, Li S, Page SJ, Shi X, Lee PD, Stevens MM, Hanna JV, Jones JR. 3D printed silica-gelatin hybrid scaffolds of specific channel sizes promote collagen Type II, Sox9 and Aggrecan production from chondrocytes. Mater Sci Eng C 2021;123:111964. https://doi.org/10.1016/j.msec.2021.111964.
[20] Robins JC, Akeno N, Mukherjee A, Dalal RR, Aronow BJ, Koopman P, Clemens TL. Hypoxia induces chondrocyte-specific gene expression in mesenchymal cells in association with transcriptional activation of Sox9. Bone 2005;37:313–22. https://doi.org/10.1016/j.bone.2005.04.040.
[21] Duval E, Baugé C, Andriamanalijaona R, Bénateau H, Leclercq S, Dutoit S, Poulain L, Galéra P, Boumédiene K. Molecular mechanism of hypoxia-induced chondrogenesis and its application in *in vivo* cartilage tissue engineering. Biomaterials 2012;33:6042–51. https://doi.org/10.1016/j.biomaterials.2012.04.061.
[22] Amarilio R, Viukov SV, Sharir A, Eshkar-Oren I, Johnson RS, Zelzer E. HIF1α regulation of Sox9 is necessary to maintain differentiation of hypoxic prechondrogenic cells during early skeletogenesis. Development 2007;134:3917–28. https://doi.org/10.1242/dev.008441.
[23] Thoms BL, Dudek KA, Lafont JE, Murphy CL. Hypoxia promotes the production and inhibits the destruction of human articular cartilage. Arthritis Rheum 2013;65:1302–12. https://doi.org/10.1002/art.37867.
[24] Dy P, Wang W, Bhattaram P, Wang Q, Wang L, Ballock RT, Lefebvre V. Sox9 directs hypertrophic maturation and blocks osteoblast differentiation of growth plate chondrocytes. Dev Cell 2012;22:597–609. https://doi.org/10.1016/j.devcel.2011.12.024.
[25] Kanichai M, Ferguson D, Prendergast PJ, Campbell VA. Hypoxia promotes chondrogenesis in rat mesenchymal stem cells: a role for AKT and hypoxia-inducible factor (HIF)-1α. J Cell Physiol 2008;216:708–15. https://doi.org/10.1002/jcp.21446.
[26] Duval E, Leclercq S, Elissalde J-M, Demoor M, Galéra P, Boumédiene K. Hypoxia-inducible factor 1α inhibits the fibroblast-like markers type I and type III collagen during hypoxia-induced chondrocyte redifferentiation: hypoxia not only induces type II collagen and aggrecan, but it also inhibits type I and type III collagen in the

hypoxia-inducible factor 1α–dependent redifferentiation of chondrocytes. Arthritis Rheum 2009;60:3038–48. https://doi.org/10.1002/art.24851.
[27] Sheehy EJ, Buckley CT, Kelly DJ. Oxygen tension regulates the osteogenic, chondrogenic and endochondral phenotype of bone marrow derived mesenchymal stem cells. Biochem Biophys Res Commun 2012;417:305–10. https://doi.org/10.1016/j.bbrc.2011.11.105.
[28] Kawato Y, Hirao M, Ebina K, Tamai N, Shi K, Hashimoto J, Yoshikawa H, Myoui A. Nkx3.2-induced suppression of Runx2 is a crucial mediator of hypoxia-dependent maintenance of chondrocyte phenotypes. Biochem Biophys Res Commun 2011; 416:205–10. https://doi.org/10.1016/j.bbrc.2011.11.026.
[29] Lafont JE, Talma S, Murphy CL. Hypoxia-inducible factor 2α is essential for hypoxic induction of the human articular chondrocyte phenotype. Arthritis Rheum 2007;56:3297–306. https://doi.org/10.1002/art.22878.
[30] Metzen E, Stiehl DP, Doege K, Marxsen JH, Hellwig-Bürgel T, Jelkmann W. Regulation of the prolyl hydroxylase domain protein 2 (phd2/egln-1) gene: identification of a functional hypoxia-responsive element. Biochem J 2005;387: 711–7. https://doi.org/10.1042/BJ20041736.
[31] Semenza GL, Roth PH, Fang HM, Wang GL. Transcriptional regulation of genes encoding glycolytic enzymes by hypoxia-inducible factor 1. J Biol Chem 1994;269: 23757–63. https://doi.org/10.1016/S0021-9258(17)31580-6.
[32] Aro E, Khatri R, Gerard-O'Riley R, Mangiavini L, Myllyharju J, Schipani E. Hypoxia-inducible Factor-1 (HIF-1) but not HIF-2 is essential for hypoxic induction of collagen prolyl 4-hydroxylases in primary newborn mouse epiphyseal growth plate chondrocytes. J Biol Chem 2012;287:37134–44. https://doi.org/10.1074/jbc.M112.352872.
[33] Kim J-H, Lee G, Won Y, Lee M, Kwak J-S, Chun C-H, Chun J-S. Matrix cross-linking–mediated mechanotransduction promotes posttraumatic osteoarthritis. Proc Natl Acad Sci U S A 2015;112:9424–9. https://doi.org/10.1073/pnas.1505700112.
[34] Makris EA, Responte DJ, Paschos NK, Hu JC, Athanasiou KA. Developing functional musculoskeletal tissues through hypoxia and lysyl oxidase-induced collagen cross-linking. Proc Natl Acad Sci USA 2014;111:E4832–41. https://doi.org/10.1073/pnas.1414271111.
[35] Maleski MP, Knudson CB. Hyaluronan-mediated aggregation of limb bud mesenchyme and mesenchymal condensation during chondrogenesis. Exp Cell Res 1996;225:55–66. https://doi.org/10.1006/excr.1996.0156.
[36] Pittenger MF, Mackay AM, Beck SC, Jaiswal RK, Douglas R, Mosca JD, Moorman MA, Simonetti DW, Craig S, Marshak DR. Multilineage potential of adult human mesenchymal stem cells. Science 1999;284:143–7. https://doi.org/10.1126/science.284.5411.143.
[37] Foyt DA, Taheem DK, Ferreira SA, Norman MDA, Petzold J, Jell G, Grigoriadis AE, Gentleman E. Hypoxia impacts human MSC response to substrate stiffness during chondrogenic differentiation. Acta Biomater 2019;89:73–83. https://doi.org/10.1016/j.actbio.2019.03.002.
[38] Erickson IE, Huang AH, Chung C, Li RT, Burdick JA, Mauck RL. Differential maturation and structure-function relationships in mesenchymal stem cell- and chondrocyte-seeded hydrogels. Tissue Eng Part A 2009;15:1041–52. https://doi.org/10.1089/ten.tea.2008.0099.
[39] Tuli R, Tuli S, Nandi S, Huang X, Manner PA, Hozack WJ, Danielson KG, Hall DJ, Tuan RS. Transforming growth factor-β-mediated chondrogenesis of human mesenchymal progenitor cells Involves N-cadherin and mitogen-activated protein kinase and Wnt signaling cross-talk. J Biol Chem 2003;278:41227–36. https://doi.org/10.1074/jbc.M305312200.
[40] Gao L, McBeath R, Chen CS. Stem cell shape regulates a chondrogenic *versus* myogenic fate through Rac1 and N-Cadherin. Stem Cells 2010;28:564–72. https://doi.org/10.1002/stem.308.
[41] Weir N, Buchanan F, Orr J, Farrar D. Influence of processing and sterilisation on properties of poly-e-caprolactone. Plast Rubber Compd 2003;32:265–70. https://doi.org/10.1179/146580103225010264.
[42] Vink P, Pleijsier K. Aeration of ethylene oxide-sterilized polymers. Biomaterials 1986;7:225–30. https://doi.org/10.1016/0142-9612(86)90108-0.
[43] Narkis M, Sibony-Chaouat S, Siegmann A, Shkolnik S, Bell JP. Irradiation effects on polycaprolactone. Polymer (Guildf) 1985;26:50–4. https://doi.org/10.1016/0032-3861(85)90056-4.
[44] Plikk P, Odelius K, Hakkarainen M, Albertsson AC. Finalizing the properties of porous scaffolds of aliphatic polyesters through radiation sterilization. Biomaterials 2006;27:5335–47. https://doi.org/10.1016/j.biomaterials.2006.06.024.
[45] Di Foggia M, Corda U, Plescia E, Taddei P, Torreggiani A. Effects of sterilisation by high-energy radiation on biomedical poly-(ε-caprolactone)/hydroxyapatite composites. J Mater Sci 2010;21:1789–97. https://doi.org/10.1007/s10856-010-4046-0.
[46] Al-Maawi S, Orlowska A, Sader R, Kirkpatrick CJ, Ghanaati S. *In vivo* cellular reactions to different biomaterials-physiological and pathological aspects and their consequences. Semin Immunol 2017;29:49–61. https://doi.org/10.1016/j.smim.2017.06.001.
[47] Modulevsky DJ, Cuerrier CM, Pelling AE. Biocompatibility of subcutaneously implanted plant-derived cellulose biomaterials. PLoS ONE 2016;11:e0157894. https://doi.org/10.1371/journal.pone.0157894.
[48] Dondossola E, Holzapfel BM, Alexander S, Filippini S, Hutmacher DW, Friedl P. Examination of the foreign body response to biomaterials by nonlinear intravital microscopy. Nat Biomed Eng 2016;1:0007. https://doi.org/10.1038/s41551-016-0007.
[49] Seyednejad H, Gawlitta D, Kuiper RV, de Bruin A, van Nostrum CF, Vermonden T, Dhert WJA, Hennink WE. *In vivo* biocompatibility and biodegradation of 3D-printed porous scaffolds based on a hydroxyl-functionalized poly(ε-caprolactone). Biomaterials 2012;33:4309–18. https://doi.org/10.1016/j.biomaterials.2012.03.002.
[50] Veiseh O, Doloff JC, Ma M, Vegas AJ, Tam HH, Bader AR, Li J, Langan E, Wyckoff J, Loo WS, Jhunjhunwala S, Chiu A, Siebert S, Tang K, Hollister-Lock J, Aresta-Dasilva S, Bochenek M, Mendoza-Elias J, Wang Y, Qi M, Lavin DM, Chen M, Dholakia N, Thakrar R, Lacík I, Weir GC, Oberholzer J, Greiner DL, Langer R, Anderson DG. Size- and shape-dependent foreign body immune response to materials implanted in rodents and non-human primates. Nat Mater 2015;14:643. https://doi.org/10.1038/nmat4290.
[51] Sridharan R, Cameron AR, Kelly DJ, Kearney CJ, O'Brien FJ. Biomaterial based modulation of macrophage polarization: a review and suggested design principles. Mater Today 2015;18:313–25. https://doi.org/10.1016/j.mattod.2015.01.019.
[52] Franz S, Rammelt S, Scharnweber D, Simon JC. Immune responses to implants – a review of the implications for the design of immunomodulatory biomaterials. Biomaterials 2011;32:6692–709. https://doi.org/10.1016/j.biomaterials.2011.05.078.
[53] Vishwakarma A, Bhise NS, Evangelista MB, Rouwkema J, Dokmeci MR, Ghaemmaghami AM, Vrana NE, Khademhosseini A. Engineering immunomodulatory biomaterials to tune the inflammatory response. Trends Biotechnol 2016;34:470–82. https://doi.org/10.1016/j.tibtech.2016.03.009.
[54] Clark JN, Garbout A, Ferreira SA, Javaheri B, Pitsillides AA, Rankin SM, Jeffers JRT, Hansen U. Propagation phase-contrast micro-computed tomography allows laboratory-based three-dimensional imaging of articular cartilage down to the cellular level. Osteoarthr Cartil 2020;28:102–11. https://doi.org/10.1016/j.joca.2019.10.007.
[55] Ferreira SA, Young G, Jones JR, Rankin S. Bioglass/carbonate apatite/collagen composite scaffold dissolution products promote human osteoblast differentiation. Mater Sci Eng C 2021;118:111393. https://doi.org/10.1016/j.msec.2020.111393.
[56] Ferreira SA, Faull PA, Seymour AJ, Yu TTL, Loaiza S, Auner HW, Snijders AP, Gentleman E. Neighboring cells override 3D hydrogel matrix cues to drive human MSC quiescence. Biomaterials 2018;176:13–23. https://doi.org/10.1016/j.biomaterials.2018.05.032.
[57] Ferreira SA, Motwani MS, Faull PA, Seymour AJ, Yu TTL, Enayati M, Taheem DK, Salzlechner C, Haghighi T, Kania EM, Oommen OP, Ahmed T, Loaiza S, Parzych K, Dazzi F, Varghese OP, Festy F, Grigoriadis AE, Auner HW, Snijders AP, Bozec L, Gentleman E. Bi-directional cell-pericellular matrix interactions direct stem cell fate. Nat Commun 2018;9:4049. https://doi.org/10.1038/s41467-018-06183-4.
[58] Xiao J, Li X, Liu J, Fan X, Lei H, Li C. Identification of reference genes in blood before and after entering the plateau for SYBR green RT-qPCR studies. PeerJ 2017; 5:e3726. https://doi.org/10.7717/peerj.3726.
[59] Legendre F, Ollitrault D, Gomez-Leduc T, Bouyoucef M, Hervieu M, Gruchy N, Mallein-Gerin F, Leclercq S, Demoor M, Galéra P. Enhanced chondrogenesis of bone marrow-derived stem cells by using a combinatory cell therapy strategy with BMP-2/TGF-β1, hypoxia, and COL1A1/HtrA1 siRNAs. Sci Rep 2017;7:3406. https://doi.org/10.1038/s41598-017-03579-y.
[60] Cao B, Li Z, Peng R, Ding J. Effects of cell–cell contact and oxygen tension on chondrogenic differentiation of stem cells. Biomaterials 2015;64:21–32. https://doi.org/10.1016/j.biomaterials.2015.06.018.
[61] Gadjanski I, Spiller K, Vunjak-Novakovic G. Time-dependent processes in stem cell-based tissue engineering of articular cartilage. Stem Cell Rev Rep 2012;8:863–81. https://doi.org/10.1007/s12015-011-9328-5.
[62] Nishioka K, Dennis JE, Gao J, Goldberg VM, Caplan AI. Sustained Wnt protein expression in chondral constructs from mesenchymal stem cells. J Cell Physiol 2005;203:6–14. https://doi.org/10.1002/jcp.20196.
[63] Cho JH, Kim SH, Park KD, Jung MC, Yang WI, Han SW, Noh JY, Lee JW. Chondrogenic differentiation of human mesenchymal stem cells using a thermosensitive poly(N-isopropylacrylamide) and water-soluble chitosan copolymer. Biomaterials 2004;25:5743–51. https://doi.org/10.1016/j.biomaterials.2004.01.051.
[64] O'Shea DG, Curtin CM, O'Brien FJ. Articulation inspired by nature: a review of biomimetic and biologically active 3D printed scaffolds for cartilage tissue engineering. Biomater Sci 2022;10:2462–83. https://doi.org/10.1039/d1bm01540k.
[65] Hu K, Olsen BR. Osteoblast-derived VEGF regulates osteoblast differentiation and bone formation during bone repair. J Clin Invest 2016;126:509–26. https://doi.org/10.1172/JCI82585.
[66] Gerber H-P, Vu TH, Ryan AM, Kowalski J, Werb Z, Ferrara N. VEGF couples hypertrophic cartilage remodeling, ossification and angiogenesis during endochondral bone formation. Nat Med 1999;5:623–8. https://doi.org/10.1038/9467.
[67] Anderson DE, Markway BD, Bond D, McCarthy HE, Johnstone B. Responses to altered oxygen tension are distinct between human stem cells of high and low chondrogenic capacity. Stem Cell Res Ther 2016;7:154. https://doi.org/10.1186/s13287-016-0419-8.
[68] Leijten J, Georgi N, Moreira Teixeira L, van Blitterswijk CA, Post JN, Karperien M. Metabolic programming of mesenchymal stromal cells by oxygen tension directs chondrogenic cell fate. Proc Natl Acad Sci USA 2014;111:13954–9. https://doi.org/10.1073/pnas.1410977111.
[69] Pattappa G, Schewior R, Hofmeister I, Seja J, Zellner J, Johnstone B, Docheva D, Angele P. Physioxia has a beneficial effect on cartilage matrix production in interleukin-1β inhibited mesenchymal stem cell chondrogenesis. Cells 2019;8:936. https://doi.org/10.3390/cells8080936.
[70] Pilgaard L, Lund P, Duroux M, Lockstone H, Taylor J, Emmersen J, Fink T, Ragoussis J, Zachar V. Transcriptional signature of human adipose tissue-derived stem cells (hASCs) preconditioned for chondrogenesis in hypoxic conditions. Exp Cell Res 2009;315:1937–52. https://doi.org/10.1016/j.yexcr.2009.01.020.

[71] Munir S, Foldager CB, Lind M, Zachar V, Søballe K, Koch TG. Hypoxia enhances chondrogenic differentiation of human adipose tissue-derived stromal cells in scaffold-free and scaffold systems. Cell Tissue Res 2014;355:89–102. https://doi.org/10.1007/s00441-013-1732-5.
[72] Kronenberg HM. Developmental regulation of the growth plate. Nature 2003;423:332–6. https://doi.org/10.1038/nature01657.
[73] Zheng Q, Zhou G, Morello R, Chen Y, Garcia-Rojas X, Lee B. Type X collagen gene regulation by Runx2 contributes directly to its hypertrophic chondrocyte-specific expression *in vivo*. J Cell Biol 2003;162:833–42. https://doi.org/10.1083/jcb.200211089.
[74] Mueller MB, Tuan RS. Functional characterization of hypertrophy in chondrogenesis of human mesenchymal stem cells. Arthritis Rheum 2008;58:1377–88. https://doi.org/10.1002/art.23370.
[75] Reboul P, Pelletier JP, Tardif G, Cloutier JM, Martel-Pelletier J. The new collagenase, collagenase-3, is expressed and synthesized by human chondrocytes but not by synoviocytes. A role in osteoarthritis. J Clin Invest 1996;97:2011–9. https://doi.org/10.1172/JCI118636.